Journal of Molecular Catalysis A: Chemical 328 (2010) 44–52

Contents lists available at ScienceDirect
Journal of Molecular Catalysis A: Chemical
journal homepage: www.elsevier.com/locate/molcata

# Enhanced photocatalytic activity of transition metal ions $Mn^{2+}$, $Ni^{2+}$ and $Zn^{2+}$ doped polycrystalline titania for the degradation of Aniline Blue under UV/solar light

L. Gomathi Devi*, Nagaraju Kottam, B. Narasimha Murthy, S. Girish Kumar

*Department of Post Graduate Studies in Chemistry, Central College City Campus, Bangalore University, Dr. Ambedkar Street, Bangalore 560001, Karnataka, India*

ARTICLE INFO

*Article history:*
Received 9 January 2010
Received in revised form 22 May 2010
Accepted 27 May 2010
Available online 4 June 2010

*Keywords:*
Transition metal ion doped $TiO_2$
Synergistic effect in the bicrystalline framework
Electronic configuration of dopant
Photocatalysis under UV/solar light
Aniline Blue

ABSTRACT

Anatase $TiO_2$ was doped with divalent transition metal ions like $Mn^{2+}$, $Ni^{2+}$ and $Zn^{2+}$ and characterized by various analytical techniques. Powder X-ray diffraction revealed stabilization of anatase phase for $Ni^{2+}$ and $Zn^{2+}$ doped samples, while phase transformation from anatase to rutile was promoted due to $Mn^{2+}$ inclusion. The rutile fraction increased with $Mn^{2+}$ concentration due to the creation of surface oxygen vacancies. All the doped catalysts showed red shift in the band gap absorption to the visible region. The photocatalytic activities of these catalysts were evaluated in the degradation of Aniline Blue (AB) under UV/solar light. Among the photocatalysts, $Mn^{2+}$ (0.06 at.%)–$TiO_2$ showed enhanced activity, which is attributed to the synergistic effect in the bicrystalline framework of anatase and rutile. Further the unique half filled electronic structure of $Mn^{2+}$ serves as a shallow trap for the charge carriers to enhance the photocatalytic activity. An insight to the mechanism of interfacial charge transfer in the mixed phase of anatase and rutile is explored, taking into consideration the theories of previous models.

## 1. Introduction

The photodegradation of organic pollutants both in air and aqueous medium catalyzed by various semiconductors is a promising remediation technology especially at lower concentration [1–10]. Among the various semiconductor used, $TiO_2$ has been recognized as one of the excellent material for its biological and chemical inertness, strong oxidizing power, cost effectiveness, long term stability against photo and chemical corrosion [11]. The photocatalytic activity of $TiO_2$ semiconductor is due to the generation of excited electrons in the conduction band and positive holes in the valence band by the absorption of UV illumination. These energetically excited species are mobile and capable of initiating surface chemical reactions, usually by the production of highly oxidative hydroxyl and superoxide radicals at the semiconductor interface. They are unstable, and recombination of electron–hole pair occurs very fast, dissipating the input energy as heat. Photocatalytic efficiency depends on the competition between these two processes, that is, the ratio of surface charge carrier transfer rate to the electron–hole pair recombination rate. If recombination process occurs too fast, the other surface chemical reactions do not occur. Furthermore, the large band gap of $TiO_2$ limits its application under solar light. Doping with transition metal ion into the $TiO_2$ matrix has been frequently reported to suppress charge carrier recombination and also for the onset shift in the band gap absorption to the visible region, thus enhancing the activity [12–22]. Paola et al. have investigated the doping of Co, Cr, Cu, Fe, Mo, V and W into $TiO_2$ matrix prepared by wet impregnation method [19]. They reported enhanced activity for W doped $TiO_2$, while other transition metal ions reduced the efficiency of $TiO_2$. Karakitsou and Verykios showed that doping with higher valent cation compared to $Ti^{4+}$ shows enhanced activity compared with lower valent cation [22]. Nagaveni et al. reported an inhibitory effect for the dopants W, V, Ce, Zr, Fe and Cu prepared by solution combustion method [21], while few researchers have claimed the enhanced activity for these dopants compared to undoped $TiO_2$ in photocatalysis [17,18,20,22]. Hence a direct comparisons and unifying conclusions cannot be made, since wide varieties of experimental conditions are employed for sample preparations and also wide variety of pollutants are chosen for the study.

The present research focuses on the doping of $Mn^{2+}$, $Ni^{2+}$ and $Zn^{2+}$ into the $TiO_2$ matrix having $d^5$, $d^8$ and $d^{10}$ electronic configuration respectively. The photocatalytic activity of these doped catalysts was evaluated in the degradation of Aniline Blue under UV/solar light. The decisive factors like nature of dopant, phase structure and dopant concentration influencing the degradation of AB were investigated in detail.

---

* Corresponding author. Tel.: +91 9845222867.
*E-mail address:* gomatidevi_naik@yahoo.co.in (L.G. Devi).

1381-1169/$ – see front matter © 2010 Published by Elsevier B.V.
doi:10.1016/j.molcata.2010.05.021

## 2. Materials and methods

Titanium tetrachloride was obtained from Merck Chemicals. Manganese oxalate, nickel oxalate, and zinc oxalate supplied from Sisco-Chem industries, Bombay was used as source for doping $Mn^{2+}$, $Ni^{2+}$ and $Zn^{2+}$ ions respectively. Aniline Blue (AB) was obtained from S D Fine Chemicals, Bombay, India, and was used as received. The molecular formula of AB is $C_{32}H_{25}N_3Na_2O_9S_3$.

### 2.1. Catalyst preparation

Crystalline anatase $TiO_2$ is prepared by sol–gel method through the hydrolysis of $TiCl_4$ [23]. 25 ml of diluted $TiCl_4$ with 1 ml concentrated $H_2SO_4$ is taken in a beaker and diluted to 1000 ml. The pH of the solution was maintained at 7–8 by adding liquor ammonia. The gel obtained was allowed to settle down. The precipitate is washed free of chloride and ammonium ions. The gelatinous precipitate is filtered and oven dried at 100 °C. The finely ground powder was then calcined at 550 °C for 4.5 h. A known concentration of the metal ion solution was added to calculated amount of $TiO_2$ to get the dopant concentration in the range of 0.02–0.1 at.%. The catalyst with dopant concentration of 0.02, 0.06 and 0.1 at.% was labeled as M-1, M-2 and M-3 respectively (where M = Mn/Zn). The dopant $Ni^{2+}$ with a concentration of 0.02, 0.08 and 0.1 at.% was labeled as Ni-1, Ni-2 and Ni-3 respectively. The mixture is ground in a mortar and oven dried at 120 °C for 1 h. The process is repeated for 3–4 times and the powder is finally calcined at 550 °C for 4.5 h.

#### 2.1.1. Analytical instruments

The crystallite phase of the sample and variation of lattice parameter upon doping with metal ions were determined by PXRD measurements using Philips powder diffractometer PW/1050/70/76 with Cu Kα radiation. The specific surface area of the powders was measured by dynamic Brunner–Emmet–Teller (BET) method in which $N_2$ gas was adsorbed at 77 K using Digisorb 2006 surface area, pore volume analyzer Nova Quanta Chrome corporation instrument multipoint BET adsorption system. The diffuse reflectance spectra (DRS) of the photocatalyst sample in the wavelength range of 200–600 nm were obtained by a UV–vis scanning spectrophotometer (31031 PC UV-VIS-NIR instrument) using $BaSO_4$ as reference standard. The band gaps of photocatalysts were calculated by using the Kubelka–Munk plot.

#### 2.1.2. Photochemical reactor

The experiments were performed in an open glass reactor (150 mm × 75 mm) whose surface area is 176 $cm^2$. A medium pressure 125 W mercury vapor lamp is used as the UV source. The photon flux of the light source is 7.75 $mW/cm^2$ as determined by ferrioxalate actinometry and the output of mercury lamp is in the range of 350–400 nm and peaks around 370 nm. In a typical experiment, 250 ml of 20 ppm AB dye solution containing 150 mg of the catalyst was magnetically stirred in dark condition for 15 min to establish an adsorption/desorption equilibrium. The difference in the concentration of substrate before and after stirring gives the amount adsorbed on the catalyst surface. All the experiments were carried out under constant stirring in the presence of atmospheric oxygen.

Experiments using solar light were carried out between 11 am and 2 pm during the summer season in Bangalore, India. At this interval the fluctuation in solar intensity was minimal. The latitudes and longitudes are 12.58 N and 77.38 E respectively. The average intensity of the sunlight is found to be around 1200 $W\,m^{-2}$. The intensity of solar light was concentrated using a convex lens and the reaction mixture was exposed to this concentrated solar light. The reaction was stirred continuously over the entire time spam of the experiment. At desired time intervals the samples were collected and centrifuged to separate the photocatalyst particles and were subjected to UV–vis spectroscopic analysis using Shimadzu UV-1700 pharmaspec UV–vis spectrophotometer.

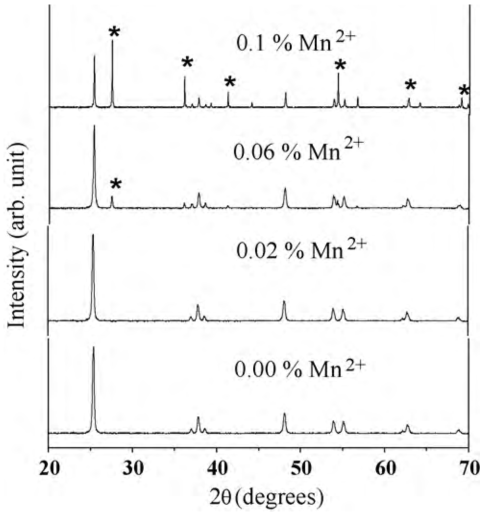

**Fig. 1.** PXRD pattern of $Mn^{2+}$–$TiO_2$ samples.

#### 2.1.3. Estimation of electrical energy per order ($E_{Eo}$)

The photodegradation of aqueous organic pollutant is a light energy driven process which can represent a major fraction of operating costs. Simple figures of merit based on the electrical energy consumption (as light energy) can therefore be very useful and informative. The appropriate figure of merit is the electrical energy per order ($E_{Eo}$), is defined as the number of kW h of electrical energy required to reduce the concentration of pollutant by one order of magnitude in 1 $m^3$ of contaminated water. $E_{Eo}$ can be calculated using Eq. (1)

$$E_{Eo} = \frac{P \times t \times 1000}{V \times 60 \times \log(C_i/C_f)} \tag{1}$$

where $P$ is the power of the light source (kW), $t$ is the irradiation time (min), $V$ is the volume of the reaction solution, $C_i$ and $C_f$ are the initial and final pollutant concentrations [24,25].

## 3. Results and discussion

### 3.1. Characterization of the photocatalyst

$Ni^{2+}$–$TiO_2$ and $Zn^{2+}$–$TiO_2$ catalysts showed anatase phase, while $Mn^{2+}$–$TiO_2$ samples exhibited bicrystalline framework of anatase and rutile. The structural changes upon doping are strongly dependent on charge and ionic radius of the dopant. The dopant with a lower charge than $Ti^{4+}$ can alter the concentration of oxygen vacancies depending on their position in $TiO_2$ matrix, they can replace Ti in $TiO_2$ lattice or can occupy interstitial position which in turn depends on their size and concentration. The ionic radii of $Ni^{2+}$ (0.72 Å) and $Zn^{2+}$ (0.74 Å) are quite similar to that of host $Ti^{4+}$ (0.68 Å) ions. Hence these ions can easily substitute $Ti^{4+}$ ion in $TiO_2$ lattice without distorting the pristine crystal structure, thereby stabilizing the anatase phase over a range of dopant concentrations.

The phase transformation from anatase to rutile was promoted by the incorporation of $Mn^{2+}$ (Fig. 1). The rutile fraction increased with increase in $Mn^{2+}$ content in the $TiO_2$ matrix. Due to the larger ionic radius of $Mn^{2+}$ (0.80 Å) compared to $Ti^{4+}$, it is impossible for $Mn^{2+}$ ions to act as interstitial ions in the $TiO_2$ matrix. Hence $Mn^{2+}$ ions can replace $Ti^{4+}$ substitutionally in the lattice sites. The substitution of metal ion with valency less than +4 and higher ionic radius would induce oxygen vacancies at the surface of anatase grains which favors the bond rupture, solid state ionic rearrangement and structure reorganization for the formation of rutile phase [26]. The rutile fraction in the sample was calculated using the Spurr and Meyer's equation: $X_R = (1 + 0.8I_A/I_R)^{-1}$, where $X_R$ is the mass fraction of rutile in the prepared samples, $I_A$ and $I_R$ were the X-ray integrated intensities corresponding to the (1 0 1) diffraction plane of anatase and (1 1 0) of rutile phase respectively [27].

At lower dopant concentration (0.02 at.%) the induced oxygen vacancies may not be sufficient to promote the phase transformation. Mn-2 shows higher anatase to rutile of 90:10, while Mn-3 shows higher rutile-to-anatase ratio of 52:48 (Fig. 1). These results suggest that phase transformation takes place smoothly at intermediate dopant concentration of 0.06 at.% and accelerates at a faster rate for higher dopant concentration. The anatase-to-rutile phase transformation is generally considered as nucleation growth process during which the rutile nuclei are formed within the anatase phase. The crystallite size of the samples was calculated using Scherrer's equation: $D = k\lambda/\beta\cos\theta$, where $k$ is the shape factor (~0.9), $\lambda$ is the X-ray wavelength (0.15418 nm), $\beta$ is the full width at half maximum (FWHM) of the diffraction line and $\theta$ is the diffraction angle. The anatase crystallite size was found to be 26.2, 23.6, 20.3 and 16.6 nm for a dopant concentration of 0.00, 0.02, 0.06 and 0.1 at.% respectively while the rutile crystallite size in the samples Mn-2 and Mn-3 were same as that of anatase. These results suggest that $Mn^{2+}$ doping into the $TiO_2$ matrix effectively inhibit the grain growth of both the phases by providing dissimilar boundaries. The anatase grain size of $TiO_2$ decreases with increase in the $Mn^{2+}$ dopant concentration due to the formation of Mn–O–Ti bonds. The decrease in the grain size increases the specific surface areas which would increase the density of surface defects at the surface of the anatase grains. The powders with smaller crystallites will have large number of lattice defects. The defect sites on the surface of anatase crystallites react with a neighboring anatase crystal with or without defect sites, the rutile nucleation may start at these sites. Further the atoms in the defect sites have higher energy than those in the main lattice and can act as nucleation sites for the rutile formation at the surface of anatase crystallites. The anatase-to-rutile phase transformation is thus promoted at these defects and then diffuses towards bulk.

The variation in the lattice parameters upon doping was reflected in the elongation of *c*-axis. Since only '*c*' dimension is changing while '*a* (=*b*)' remains almost constant for the range of dopant concentration, it can be concluded that $Mn^{2+}$ substitutes $Ti^{4+}$ preferentially on the bcc and fcc in the anatase structure [28]. The substitution of $M^{2+}$ (M = Mn, Ni and Zn) ions in the $TiO_2$ lattice follows Vegard's law which states that "Change in the unit cell dimension will be linear with respect to the change in composition" which confirms the incorporation of the dopant in the substitutional site.

### 3.2. Optical electronic properties

The intensity of the reflected radiation provides information about the wavelength at which semiconductor absorbs the light. The UV–vis absorption spectra are shown in Fig. 2. The absorption band in the UV region (~380 nm) can be attributed to the band gap excitation of anatase $TiO_2$ which corresponds to band to band transition from Ti 3d to O 2p levels. The doped samples showed a significant shift in the band gap absorption to the longer wavelength, due to the introduction of electronic level which forms lowest unoccupied molecular orbital within the band gap states of $TiO_2$ (Fig. 3A). Introduction of such energy levels within the band gap states induces red shift in the absorption and endows the resulting catalysts with solar light harvesting capacity. The light absorption ability increased with increase in the dopant concentration and a blue shift was observed at higher dopant concentration (~0.1 at.%) which is consistent with previous reports [29–32]. Both $Mn^{2+}$ and $Zn^{2+}$ doped samples showed maximum band gap absorption values at ~456 nm at a dopant concentration of 0.06 at.%, while $Ni^{2+}$ doped samples displayed strong visible absorption band at 468 nm at 0.08 at.%. The absorption band in the visible region can also arise due to d–d transition of metal ions or charge transfer transition between the interacting ions [33,34].

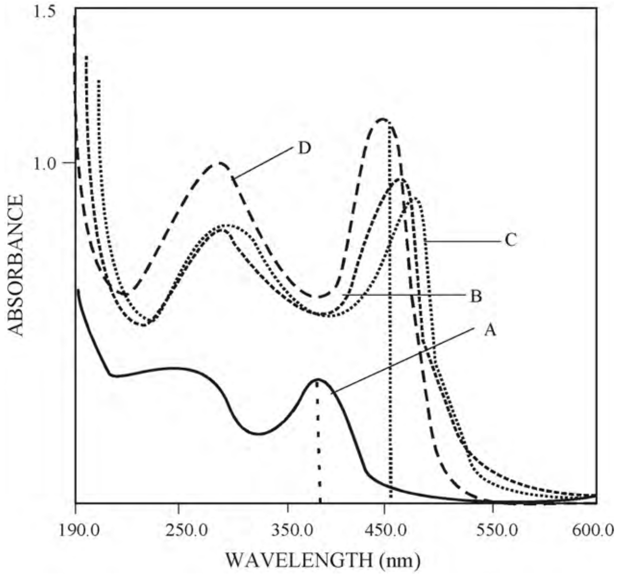

Fig. 2. UV–vis absorption spectra of photocatalysts. (A) $TiO_2$, (B) $Mn^{2+}$ (0.06 at.%)–$TiO_2$, (C) $Ni^{2+}$ (0.08 at.%)–$TiO_2$, (D) $Zn^{2+}$ (0.06 at.%)–$TiO_2$.

$$M^{n+} + M^{n+} \rightarrow M^{(n+1)+} + M^{(n-1)+} \tag{2}$$

The similarity in the band gap absorption values for $Mn^{2+}$ and $Zn^{2+}$ doped samples and a slight higher band gap absorption value for $Ni^{2+}$–$TiO_2$ sample can be explained by taking into consideration, the electronegativity of doped metal atoms. Hur et al. reported the visible light photocatalytic activity of strontium indium niobate doped with $Pb^{4+}$ and $Sn^{4+}$ for the degradation of 4-chlorophenol. Since the substituted $Pb^{4+}$ and $Sn^{4+}$ are more electronegative than $In^{3+}$, the Pb 6s and Sn 5s electronic states were expected to have lower energy than In 5s electronic state. The large shift in the band gap absorption in $Pb^{4+}$ doped samples compared to $Sn^{4+}$, was attributed to higher electronegativity of $Pb^{4+}$ in comparison with $Sn^{4+}$ [35]. The similar red shift in the band gap absorption values of Zn and V doped $TiO_2$ was mainly attributed to the similarity in the electronegativity of both the dopants [36]. Further, large shift in the band gap absorption for Mo doped $TiO_2$ in comparison with Mn doped $TiO_2$ was accounted to the higher electronegativity of Mo [37]. Hence, we speculate that higher electronegativity of Ni compared to Zn

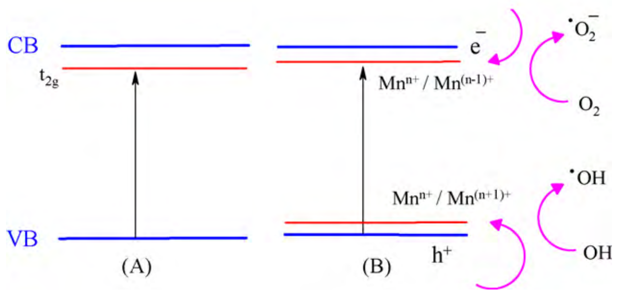

Fig. 3. Visible light activated doped catalyst (A) and charge carrier trapping mechanism in doped catalyst (B).

**Table 1**
Detailed characterization of doped titania.

| Photocatalyst | Phase fraction A:R | $C^a$ (nm) | Lattice parameter (Å) | $\lambda^b$ (nm) | $E_g^c$ (eV) | SA[d] |
|---|---|---|---|---|---|---|
| $TiO_2$ | 100:0 | 26.3 | $a=b=3.7828$, $c=9.5023$ | 380 | 3.2 | 18 |
| Mn-1 | 100:0 | 23.6 | $a=b=3.7832$, $c=9.5103$ | 426 | 2.9 | 21 |
| Mn-2 | 90:10 | 20.3:20.3$^R$ | $a=b=3.7824$, $c=9.5211$ | 454 | 2.7 | 26 |
| Mn-3 | 52:48 | 16.6:16.6 $^R$ | $a=b=3.7800$, $c=9.5002$ | 420 | 2.9 | 24 |
| Ni-1 | 100:0 | 23.8 | $a=b=3.7832$, $c=9.5069$ | 426 | 2.9 | 25 |
| Ni-2 | 100:0 | 18.9 | $a=b=3.7800$, $c=9.5189$ | 468 | 2.6 | 30 |
| Ni-3 | 100:0 | 15.1 | $a=b=3.7800$, $c=9.5228$ | 450 | 2.7 | 31 |
| Zn-1 | 100:0 | 23.6 | $a=b=3.7832$, $c=9.5123$ | 420 | 2.9 | 25 |
| Zn-2 | 100:0 | 19.8 | $a=b=3.7824$, $c=9.5311$ | 456 | 2.7 | 32 |
| Zn-3 | 100:0 | 15.6 | $a=b=3.7820$, $c=9.5009$ | 442 | 2.8 | 37 |

A:R anatase:rutile ratio.
[a] Crystallite size calculated from Scherrer's equation.
[b] Band gap absorption values calculated from UV–vis absorption spectroscopy.
[c] Mid band gap states estimated from Kubelka–Munk method.
[d] Specific surface area estimated from BET surface area analysis.

and Mn resulted in the large shift in the band gap absorption, while similar electronegativity of Mn and Zn resulted in almost similar shift in the band gap absorption values. The electronic states of and Ni were found to be at ~0.6 eV and while for Mn and Zn, it was at ~0.5 eV below the conduction band edge of $TiO_2$, as determined by Kubelka–Munk plot. The results are shown in Table 1.

### 3.3. Induced defect states by the dopant in the pristine $TiO_2$

The variable oxidation states and their ionic radii of Mn are $Mn^{2+}$ (0.80 Å), $Mn^{3+}$ (0.66 Å) or $Mn^{4+}$ (0.60 Å). Probable defect states can be represented using Kroger and Vink notation [38,39]

Assuming $Mn^{4+}$ occupying the lattice position of $Ti^{4+}$ in $TiO_2$ matrix:

$$MnO_2 \leftrightarrow Mn_{Ti} + 2O_o(\mathrm{Mnisin+4oxidationstate}) \quad (3)$$

Assuming $Mn^{3+}/Mn^{2+}$ occupying the lattice position of $Ti^{4+}$ in $TiO_2$ matrix, it induces doubly ionized/two singly ionized oxygen vacancies:

$$Mn_2O_3 \leftrightarrow 2Mn''_{Ti} + 3O_o + V_o^{\bullet\bullet}/2V_o^{\bullet} \quad (\mathrm{Mn\ in+3\ oxidation\ state}) \quad (4)$$

$$MnO \leftrightarrow Mn''_{Ti} + O_o + V_o^{\bullet\bullet}/2V_o^{\bullet} \quad (\mathrm{Mn\ is\ in+2\ oxidation\ state}) \quad (5)$$

$$ZnO \leftrightarrow Zn''_{Ti} + O_o + V_o^{\bullet\bullet}/2V_o^{\bullet} \quad (\mathrm{Zn\ is\ in+2\ oxidation\ state}) \quad (6)$$

$$NiO \leftrightarrow Ni''_{Ti} + O_o + V_o^{\bullet\bullet}/2V_o^{\bullet} \quad (\mathrm{Ni\ is\ in+2\ oxidation\ state}) \quad (7)$$

The ionized oxygen vacancies induced by $Ni^{2+}$ and $Zn^{2+}$ is assumed to be negligible due to the absence of rutile phase in the doped samples.

Charge compensation can also occur by interstitial oxygen which is less probable due to the higher ionic size of oxygen:

$$Mn_2O_3 \leftrightarrow 2Mn''_{Ti} + O''_i + 2O_o \quad (\mathrm{Mn\ is\ in+3\ oxidation\ state}) \quad (8)$$

$$MnO \leftrightarrow Mn''_{Ti} + O''_i \quad (\mathrm{Mn\ is\ in+2\ oxidation\ state}) \quad (9)$$

$$ZnO \leftrightarrow Zn''_{Ti} + O''_i \quad (\mathrm{Zn\ is\ in+2\ oxidation\ state}) \quad (10)$$

$$NiO \leftrightarrow Ni''_{Ti} + O''_i \quad (\mathrm{Ni\ is\ in+2\ oxidation\ state}) \quad (11)$$

The notations $V_o$, $V_o^{\bullet}$ and $V_o^{\bullet\bullet}$ represent neutral, single and doubly ionized oxygen vacancies. $O_o$ is oxygen occupying oxygen lattice site. $Mn_{Ti}$ is manganese ion at titanium lattice site and the (′) represents the deficiency in the charge.

### 3.4. FT-IR analysis

FT-IR studies with KBr as reference standard shows the following results:

1. Undoped $TiO_2$ shows strong absorption bands at 482 and 560 cm$^{-1}$ which can be assigned to Ti–O and Ti–O–Ti bond in the $TiO_2$ lattice. The peaks at 850 and 915 cm$^{-1}$ may be assigned to stretching vibrations of O–O for peroxo groups and vibrations of Ti–O–O bond [37].
2. The bands at 3432 and 1655 cm$^{-1}$ for all the photocatalysts were attributed to the surface adsorbed water molecules and Ti–OH bonding vibration [40].
3. On doping, the band at 560 cm$^{-1}$ shifts towards lower frequencies suggesting the possible formation of M–O–Ti bond ($M = Mn^{2+}$, $Ni^{2+}$, and $Zn^{2+}$).
4. The catalyst Mn-2 showed additional band at 460 cm$^{-1}$ corresponding to rutile framework of O–Ti–O bond [41].
5. The band at 460 cm$^{-1}$ increased in its intensity for the catalyst Mn-3 which confirms the higher fraction of rutile present in the sample compared to Mn-2, which is in agreement with the PXRD pattern.
6. The intensity of the bands at ~3432 and ~1655 cm$^{-1}$ significantly reduced in its intensity with increase in the concentration of the dopants ($Mn^{2+}$, $Ni^{2+}$ and $Zn^{2+}$) and broadening of the bands were observed owing to decrease in the crystallite size of the doped samples. The decrease in the intensity of the bands suggests the possible interaction of dopants with surface hydroxyl groups of pristine $TiO_2$.

## 4. Photocatalytic activity

### 4.1. Photocatalytic degradation of Aniline Blue (AB)

The efficiencies of the photocatalysts were tested for the degradation of AB under UV/solar light. The photolysis of dye under both UV/solar light was negligible and no degradation of the dye took place in the presence of catalyst without light irradiation. Hence the degradation of AB was mainly due to the combined effect of catalyst and light irradiation. The concentration of AB decreased monotonically during the course of reaction. The doped catalyst at

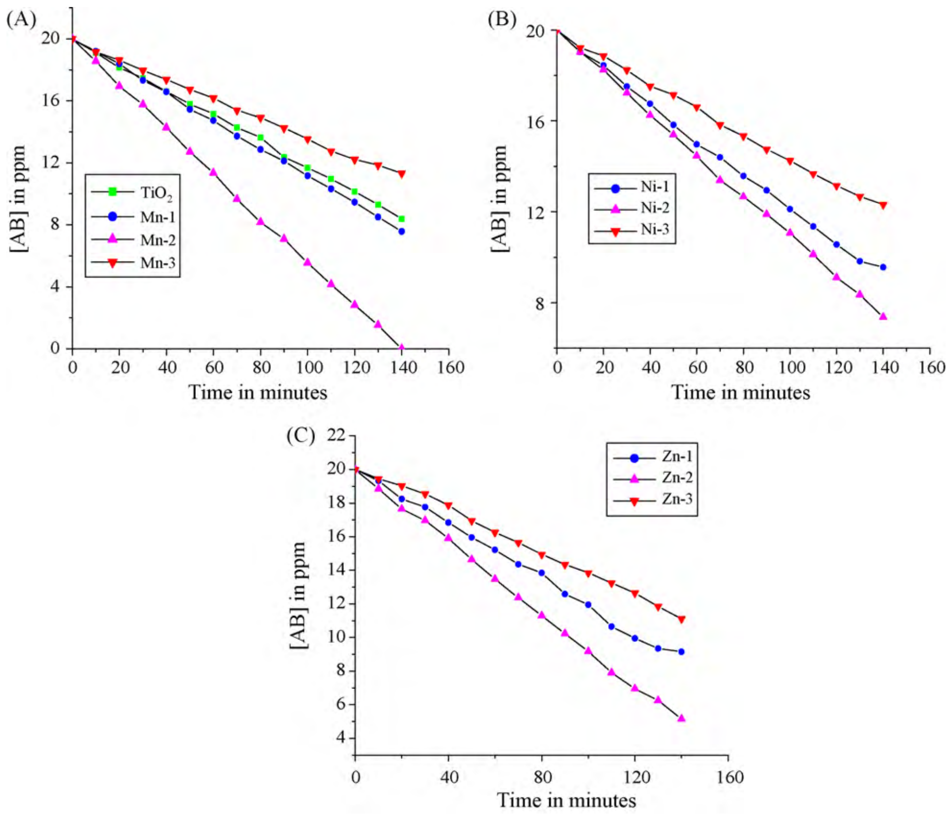

**Fig. 4.** Concentration versus time plot for the degradation of AB using all various photocatalysts under UV light.

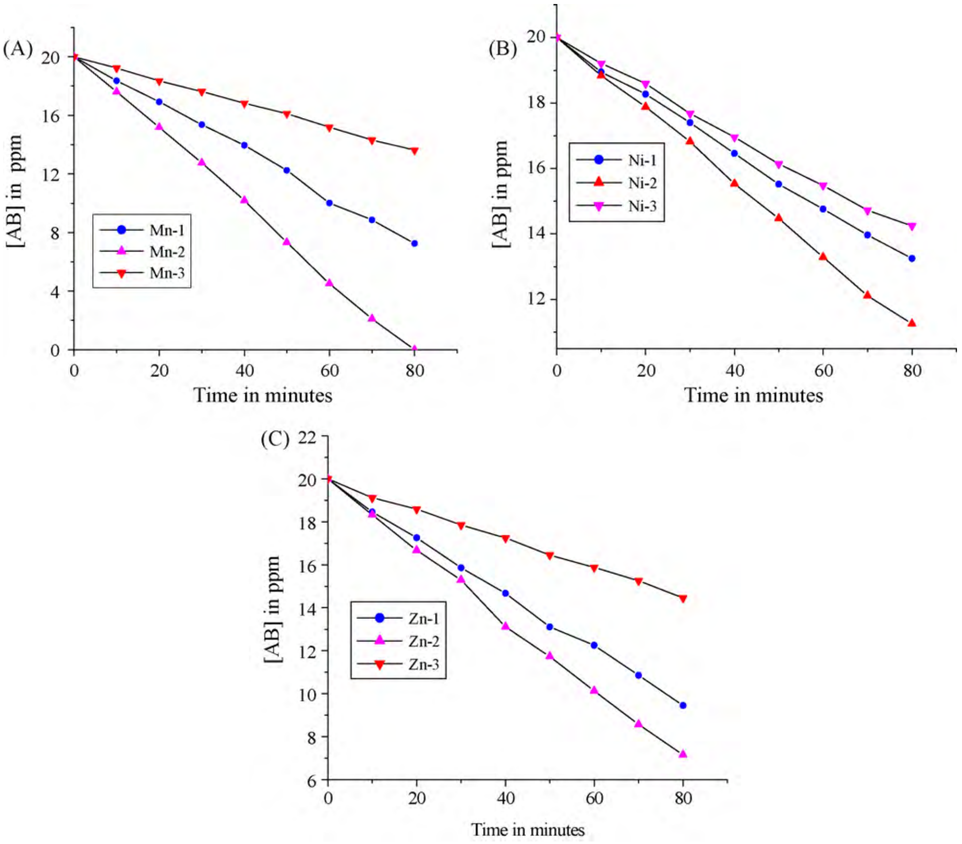

**Fig. 5.** Concentration versus time plot for the degradation of AB using all various photocatalysts under solar light.

an optimum dopant concentration showed considerably enhanced activity compared to pure $TiO_2$ indicating that localized electronic states of the dopant served as charge carrier traps for the photogenerated charge carriers under both UV/solar light illumination. The dopant within the $TiO_2$ matrix can act as trap sites for both electron and hole depending on its energy level which can be either below conduction band or just above the valence band (Fig. 3B). Plot of $C/C_0$ versus time for the degradation of AB with different photocatalysts are shown in Figs. 4 and 5.

Mn-2 showed enhanced activity compared to Ni and Zn doped catalysts. The complete degradation of AB was achieved in 140/80 min under UV/solar irradiation, suggesting the fact that, intermediates formed was destroyed at a faster rate under solar light illumination. There was continuous decrease in the $\lambda_{max}$ of the dye during the course of the reaction. The decrease was faster in the solar light photocatalysis compared to UV light photocatalysis. New bands appeared in the UV–vis spectra (270–360 nm) corresponding to the formation of substituted aromatic compounds at 90 min under UV irradiation, however no new bands appeared for 60 min of solar illumination confirming that the intermediates were rapidly degraded under solar light (UV–vis spectra not shown). The rate constant values calculated from the plot of $-\log C/C_0$ versus time using all the photocatalyst are shown in Table 2. The photocatalytic activity depends on several factors like surface area, phase structure, crystallite size, band gap, etc. Although Ni-2 showed largest shift in the band gap, the rate constant calculated was found to be 2.6/4.4 times lower under UV/solar light compared to Mn-2. It is commonly accepted that narrower band gap corresponds to less powerful redox ability [42], because the photocatalytic system can be assumed to be an electrochemical cell, the large decrease in the band gap results in lower oxidation–reduction potential based on Eq. (12).

$$\Delta G = -nFE \tag{12}$$

$\Delta G$ is the free energy change of the redox process occurring in the system, $n$ is the number of electrons involved in the redox process, $F$ is the Faraday constant and $E$ represents the band gap of the semiconductor. This indicates that the large band gap narrowing in the case of $Ni^{2+}$ doped sample is unfavorable for the photocatalytic activity.

Secondly Ni and Zn doped $TiO_2$ samples showed larger surface area, still its photocatalytic activity was low compared to Mn-2. Larger surface area may be an important factor for the photocatalytic degradation reactions, as large amount of pollutant can be adsorbed promoting the interfacial charge transfer rate. However the catalyst with larger surface area is usually associated with large amount of crystalline defects favoring the recombination of photogenerated charge carriers and leading to low photocatalytic activity [43]. Hence larger surface area is a requirement but not a decisive factor. The band gap shift to the visible region for Mn-2, Ni-3 and Zn-2 were almost same, but photocatalytic activity varied to a larger extent. Further the rate constant calculated for Mn-2 was higher compared to Mn-3 despite the fact that both the photocatalyst had similar specific surface area. From the above results, it cannot be concluded that, neither the surface area nor the band gap absorption had any obvious relation on the enhanced photocatalytic activity in the present study.

The enhanced activity of Mn-2 under both UV/solar light was critically attributed to the bicrystalline framework of anatase and rutile which suggests the existence of synergistic effect between the mixed polymorphs. It is well known that $TiO_2$ with bicrystalline framework of anatase-rutile or rutile-brookite or anatase-brookite can effectively reduce the recombination of photogenerated charge carrier enhancing the photocatalytic activity [44–69].

Under UV light excitation, anatase in the mixed phase gets activated as it is a good absorber of UV light photons. The vectorial electron transfer takes place from the conduction band edge of anatase-to-rutile electron-trapping sites. Thus rutile serves as passive electron sink hindering the recombination in anatase phase and the hole originated from the anatase transfers to the surface [70]. Subsequent electron transfer to impurity level of the dopant which lies ∼0.5 eV below the conduction band of rutile favors effective charge separation accelerating the interfacial charge transfer process which accounts for higher efficiency of Mn-2 compared to other photocatalyst under UV light (Fig. 6).

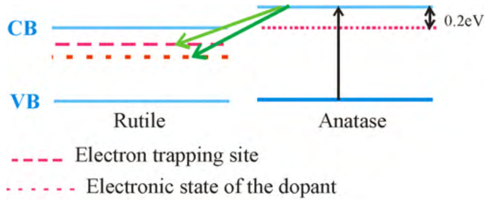

**Fig. 6.** Mechanism of interfacial charge transfer in the bicrystalline framework of anatase and rutile under UV light irradiation.

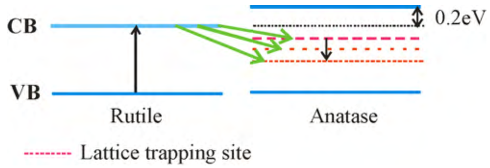

**Fig. 7.** Mechanism of interfacial charge transfer in the bicrystalline framework of anatase and rutile under solar light irradiation.

The band gap of rutile is favorable for visible light excitation as the conduction band edge of rutile lie ∼0.2 eV below the conduction band edge of anatase. Under visible light excitation, the photogenerated electron from conduction band of rutile vectorially transfers to electron-trapping sites of anatase phase (Fig. 7). This can be considered as antenna effect by rutile phase [71]. Subsequent transfer of electrons to lattice trapping sites of anatase/impurity level of the dopant further separates the charge carriers effectively. The lattice trapping sites of anatase has energy of 0.8 eV less than the conduction band edge of anatase [72]. Thus by competing with the charge carrier recombination, the charge separation activates the catalyst and the hole originating from the rutile valence band participates in the degradation mechanism.

In order for such an effective interparticle electron transfer to be possible, the two polymorphs must be in close contact which mainly depends on their crystallite size. Hong et al. prepared iodine-doped titania with mixed phases of anatase and rutile by calcining the sample at 500 °C, which showed lower activity compared to iodine-doped anatase titania. The low activity was attributed to the large rutile crystal size compared to anatase which resulted in poor intimate contact between the mixed phases [73]. Hence it is crucial to maintain the crystallite size of both the phases which enables the mixed phase for efficient charge transfer. The sample Mn-2 has anatase-to-rutile ratio of 90:10 and the crystallite size is 20.3 nm for both the phases. Since the crystallite size of both the phases is same, it can be speculated that the both the polymorphs are in intimate contact. According to Gray et al., such an interfacial mixed polymorph structure would contain a surplus amount of tetrahedral $Ti^{4+}$ sites which can act as reactive electron-trapping sites. These isolated tetrahedral $Ti^{4+}$ sites are more active than octahedrally coordinated $Ti^{4+}$ sites as in bulk $TiO_2$ [74]. These tetrahedral $Ti^{4+}$ sites could serve as catalytic hot spots at anatase/rutile interface and thus avails the mixed polymorph nanocrystals into an effective photocatalytic relay for solar energy utilization. Hence we believe that these tetrahedral $Ti^{4+}$ sites contribute to the increased activity of the mixed phase relative to the pure anatase (Mn-1).

**Table 2**

Percentage degradation ($D$), first order rate constant ($k$) and estimation of electrical energy per order ($E_{\mathrm{Eo}}$) for the degradation of AB using various photocatalysts.

| Photocatalyst | UV light irradiation[a] | | | Solar light irradiation[b] | | |
|---|---|---|---|---|---|---|
| | $D$[c] | $k$ | $E_{\mathrm{Eo}}$ | $D$[c] | $k$ | $E_{\mathrm{Eo}}$ |
| $TiO_2$ | 58 | 0.61 | 2.58 | 05 | – | – |
| Mn-1 | 62 | 0.69 | 2.30 | 65 | 1.32 | 12.10 |
| Mn-2 | 100 | 1.84 | 0.80 | 100 | 3.33 | 4.77 |
| Mn-3 | 45 | 0.41 | 3.93 | 32 | 0.49 | 32.07 |
| Ni-1 | 55 | 0.54 | 3.03 | 35 | 0.52 | 29.82 |
| Ni-2 | 63 | 0.70 | 2.23 | 45 | 0.75 | 21.35 |
| Ni-3 | 40 | 0.35 | 4.62 | 30 | 0.44 | 36.23 |
| Zn-1 | 58 | 0.60 | 2.86 | 53 | 0.93 | 16.37 |
| Zn-2 | 75 | 0.97 | 1.65 | 65 | 1.34 | 11.92 |
| Zn-3 | 44 | 0.42 | 3.80 | 28 | 0.39 | 37.79 |

[a] Illumination time period of 140 min.

[b] Illumination time period of 80 min.

[c] First order rate constant in $10^{-2}$ min$^{-1}$ calculated from the plot of $-\log C/C_0$ versus time.

The small crystallite size in Mn-2 reduces the diffusion path length for the charge carriers, from the site where they are photo produced to the site where they react. Reduction in this diffusion path length results in reduced recombination of charge carriers resulting in enhanced interfacial charge transfer process. Therefore such an intimate contact between the mixed polymorph with smaller crystallite will have a core of rutile crystallites interwoven with bound anatase crystallites, thus accelerating the transfer of electrons from rutile to neighboring anatase sites or to the impurity level created by the dopants. However it is vital that the existence of synergistic effect between the mixed polymorphs is not universal and there exist an optimum value for both the phases to show enhanced activity. In the present case optimum value was found to be an anatase-to-rutile ratio of 90:10.

With the dopant concentration around 0.1 at.%, the crystallite size for both the phases is found to be 16.6 nm in Mn-3. In these crystallites most of the charge carriers are generated sufficiently close to the surface. As a result, the photogenerated charge carriers may quickly reach the surface resulting in faster surface recombination reaction. This is also due to the excess trapping sites in the sample and lack of driving force to separate these charge carriers. In the catalyst with smaller crystallite size, surface charge carrier recombination reaction prevails over interfacial charge transfer process. Since $Mn^{2+}$ serves as trapping site for both electron and hole, the possibilities of trapping both the charge carriers will be high at higher dopant concentration and this trapped charge carrier may recombine through quantum tunneling [75]. Therefore there is a need for optimal dopant concentration in the $TiO_2$ matrix to get effective crystallite size for highest photo catalytic efficiency. Beyond the optimum dopant concentration, the rate of recombination starts dominating the reaction in accordance with Eq. (13)

$$K_{\mathrm{RR}} \propto \exp\frac{-2R}{a_0} \tag{13}$$

where $K_{\mathrm{RR}}$ is the rate of recombination, $R$ is the distance separating the electrons and hole pairs, $a_0$ is the hydrogenic radius of the wave function for the charge carrier. As a consequence the recombination rate increases exponentially with the dopant concentration because the average distance between the trap sites decreases with increasing number of dopant ions confined with in a particle. Further it is suggested that $Ti^{4+}$ in the $TiO_2$ with higher fraction of rutile is more difficult to be reduced to $Ti^{3+}$ which suggests that trapping sites might serve as recombination centers which is in agreement with above Eq. (13).

Pleskov reported that the value of space charge region potential for the effective separation of photogenerated charge carriers must not be lower than 0.2 eV [76]. On this basis, it can be concluded that there exist an optimum dopant concentration in the $TiO_2$ matrix to prolong the separation of photogenerated charge carriers. Furthermore, the thickness of space charge layer is affected by dopant content in according to the following equation:

$$W = \left(\frac{2\varepsilon\varepsilon_0 V_{\mathrm{s}}}{eN_{\mathrm{d}}}\right)^{1/2} \tag{14}$$

where '$W$' is the thickness of space charge layer, $\varepsilon$ and $\varepsilon_0$ are the static dielectric constants of the semiconductor and of the vacuum, $V_{\mathrm{s}}$ is the surface potential, $N_{\mathrm{d}}$ is the number of dopant donor atoms, $e$ is the electronic charge. The above equation clearly shows that $W$ decreases as the dopant content increases [77]. In addition, penetration depth $l$, of the light into the solid is given by $l = 1/a$, in which '$a$' is the light absorption coefficient at a given wavelength which decreases with increase in dopant concentration [78]. When the value of $W$ approximates that of $l$, all the photons absorbed generate electron–hole pairs that are efficiently separated. Consequently it is understandable that the existence of optimum value of $N_{\mathrm{d}}$ for which a space charge exist whose electric force is not less than 0.2 eV and whose thickness is more or less equal to light penetration depth [77]. For higher dopant concentration, the band bending may occur in a thin layer near the surface, so that most of particle interior will be lacking in potential drop. Hence the space charge region becomes narrow and the penetration depth of light into $TiO_2$ greatly exceeds the thickness of the space charge layer which increases the recombination rate of electrons and holes. Moreover, at a high dopant concentration, the charge carriers may be trapped more than once on its way to the surface so that their mobility becomes extremely low and undergoes recombination before it can reach the surface [75,79]. In addition at higher concentrations, these trap centers are close to one another and the trapped charge carriers can recombine through quantum tunneling, the probability of which increases with increase in the dopant concentration.

### 4.2. *Trapping and detrapping of charge carriers*

The dopant inside the $TiO_2$ matrix can serve as electron trap, if their energy level is just below conduction band or hole trap, if their energy level is just above the valence band (Fig. 3a). $Mn^{2+}$ has valence electronic configuration of $3d^5$. When these dopant ions trap electron/hole, there will be considerable loss of spin energy, as spin states changes from high spin (five unpaired electrons) to low spin (four unpaired electrons). According to crystal field theory, the trapped electron/hole will be transferred to surface adsorbed water molecules to restore its energy (Fig. 8), thereby suppressing the recombination of photogenerated electron–hole pairs [78]. Since both the oxidation states are highly unstable, the trapped electron will be transferred to oxygen molecule and trapped hole to surface adsorbed water molecules or to dye molecule.

$$Mn^{2+} + e^- \rightarrow Mn^+ \tag{15}$$

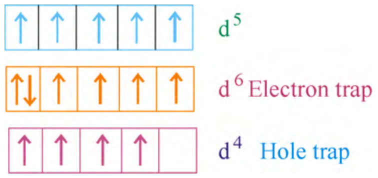

**Fig. 8.** Electron/hole trap in metal ion having half filled electronic configuration as per Ref. [78].

$$Mn^{+} + O_{2ads} \rightarrow Mn^{2+} + O_2^{\bullet -} \tag{16}$$

$$Mn^{2+} + h^{+} \rightarrow Mn^{3+} \tag{17}$$

$$Mn^{3+} + OH^{-} \rightarrow Mn^{2+} + OH^{\bullet} \tag{18}$$

Alternatively, the $Mn^{3+}$ can also trap conduction band electron or $Mn^{+}$ can trap valence band hole to retain half filled electronic structure of $Mn^{2+}$

$$Mn^{+} + h^{+} \rightarrow Mn^{2+} \tag{19}$$

$$Mn^{3+} + e^{-} \rightarrow Mn^{2+} \tag{20}$$

The dopants $Ni^{2+}$ and $Zn^{2+}$ also exhibit similar trapping and detrapping mechanism.

$$Ni^{2+} + e^{-} \rightarrow Ni^{+} \tag{21}$$

$$Ni^{+} + O_{2ads} \rightarrow Ni^{2+} + O_2^{\bullet -} \tag{22}$$

$$Ni^{+} + h^{+} \rightarrow Ni^{2+} \tag{23}$$

$$Ni^{2+} + h^{+} \rightarrow Ni^{3+} \tag{24}$$

$$Ni^{3+} + OH^{-} \rightarrow Ni^{2+} + OH^{\bullet} \tag{25}$$

$$Ni^{3+} + e^{-} \rightarrow Ni^{2+} \tag{26}$$

$$Zn^{2+} + e^{-} \rightarrow Zn^{+} \tag{27}$$

$$Zn^{+} + O_{2ads} \rightarrow Zn^{2+} + O_2^{\bullet -} \tag{28}$$

$$Zn^{+} + h^{+} \rightarrow Zn^{2+} \tag{29}$$

$$Zn^{2+} + h^{+} \rightarrow Zn^{3+} \tag{30}$$

$$Zn^{3+} + OH^{-} \rightarrow Zn^{2+} + OH^{\bullet} \tag{31}$$

$$Zn^{3+} + e^{-} \rightarrow Zn^{2+} \tag{32}$$

Choi. et al has reported the photocatalytic activities of quantum sized $TiO_2$ doped with different transition metal ions for the oxidation of chloroform and reduction of carbon tetrachloride. They have reported the enhanced photo activity for $Fe^{3+}$ doped samples which have stable half filled electronic configuration [80]. Xu et al. have also reported the influence of doping different rare earth metal ions into the $TiO_2$ lattice for the decomposition of nitrate. They have reported the enhanced activity of $TiO_2$ doped with $Gd^{3+}$ ions which also possess stable half filled electronic configuration [81]. In the line of this reasoning, we also attribute to the enhanced activity of $Mn^{2+}$ to its half filled electronic structure, which serves as shallow trap for the charge carriers to accelerate interfacial charge transfer processes. These processes not only accelerate interfacial charge transfer process, but also enhance the generation of highly reactive oxidative species like superoxide and hydroxyl radicals.

## 5. Conclusion

Anatase $TiO_2$ was doped with divalent transition metal ions like $Mn^{2+}$, $Ni^{2+}$ and $Zn^{2+}$ and their photocatalytic activity was probed in the degradation of AB under UV/solar light. The dopant $Ni^{2+}$ and $Zn^{2+}$ metal ions stabilized anatase phase, while $Mn^{2+}$ promoted phase transformation to rutile due to creation of surface oxygen vacancies. Among the photocatalysts used, $Mn^{2+}$ (0.06 at.%)–$TiO_2$ showed enhanced activity both under UV/solar light due to: (i) synergistic effect in the bicrystalline framework of anatase and rutile; (ii) smaller crystallite size with high intimate contact between the mixed phases which facilitate effective interparticle electron transfer; (iii) half filled electronic structure of $Mn^{2+}$, which serves as shallow trap for the charge carriers.

## Acknowledgement

Financial support from UGC Major Research Project (2007–2010) is acknowledged.

## References

[1] J. Yu, H. Yu, B. Cheng, J. Mol. Catal. A: Chem. 249 (2006) 135–142.
[2] J. Yu, L. Zhang, B. Cheng, Y. Su, J. Phys. Chem. C 111 (2007) 10582–10589.
[3] J. Yu, W. Liu, H. Yu, Cryst. Growth Des. 8 (2008) 930–934.
[4] J. Yu, Y. Su, B. Cheng, Adv. Funct. Mater. 17 (2007) 1984–1990.
[5] J. Yu, G. Wang, B. Cheng, M. Zhou, Appl. Catal. B: Environ. 69 (2007) 171–180.
[6] J. Yu, S. Liu, H. Yu, J. Catal. 249 (2007) 59–66.
[7] M.N. Abellan, B. Bayarri, J. Gimenez, J. Costa, Appl. Catal. B: Environ. 74 (2007) 233–241.
[8] Z. Pengyi, L. Fuyan, Y. Gang, C. Qing, Z. Wenpeng, J. Photochem. Photobiol. A: Chem. 156 (2009) 189–194.
[9] J. Yu, X. Yu, Environ. Sci. Technol. 42 (2008) 4902–4907.
[10] J. Yu, X. Yu, B. Huang, X. Zhang, Y. Dai, Cryst. Growth Des. 9 (2009) 1474–1480.
[11] M.A. Fox, M.T. Dulay, Chem. Rev. 93 (1993) 341–357.
[12] S.T. Martin, C.L. Morrison, M.R. Hoffmann, J. Phys. Chem. 98 (1994) 13695–13704.
[13] L. Palmisano, L.V. Augugliaro, A. Sclafani, M. Schiavello, J. Phys. Chem. 92 (1988) 6710–6713.
[14] C. Martin, I. Maritn, V. Rives, L. Palmisano, M. Schiavell, J. Catal. 134 (1992) 434–444.
[15] J. Soria, J.C. Conesa, V. Augugliaro, L. Palmisano, M. Schiavello, A. Sclafani, J. Phys. Chem. 95 (1991) 274–282.
[16] S. Kim, S.J. Hwang, W. Choi, J. Phys. Chem. B 109 (2005) 24260–24267.
[17] M. Zhou, J. Yu, B. Cheng, J. Hazard. Mater. 137 (2006) 1838–1847.
[18] H.W. Slamet, E. Nasution, S. Purnama, J. Gunlazuardi, Catal. Commun. 6 (2005) 313–319.
[19] A.D. Paola, G. Marci, L. Palmisano, M. Schiavello, K. Uosaki, S. Ikeda, B. Ohtani, J. Phys. Chem. B 106 (2002) 637–645.
[20] J. Arana, G. Diaz, M.M. Saracho, J.M.D. Rodriguez, J.A.H. Melian, J.P. Pena, Appl. Catal. B: Environ. 36 (2002) 113–124.
[21] K. Nagaveni, M.S. Hegde, G. Madras, J. Phys. Chem. B 108 (2004) 20204–20212.
[22] K.E. Karakitsou, X.E. Verykios, J. Phys. Chem. 97 (1993) 1184–1189.
[23] L.G. Devi, G.M. Krishnaiah, J. Photochem. Photobiol. A: Chem. 121 (1999) 141–145.
[24] N. Daneshvar, A. Aleboyeh, A.R. Khataee, Chemosphere 59 (2005) 761–767.
[25] J.R. Bolton, K.G. Bircger, W. Tumas, C.A. Tolman, Pure Appl. Chem. 73 (2001) 627–637.
[26] H.E. Chao, Y.U. Yun, H.U. Xingfang, A. Larbot, J. Eur. Ceram. Soc. 23 (2003) 1457–1464.
[27] R. Spurr, W. Myers, Anal. Chem. 29 (1957) 760–762.
[28] A. Burns, G. Hayes, W. Li, J. Hirvonen, J.D. Demaree, I.S. Shah, Mater. Sci. Eng. B 111 (2004) 150–155.
[29] Y. Yang, X.J. Li, J.T. Chen, L.Y. Wang, J. Photochem. Photobiol. A: Chem. 163 (2004) 517–522.
[30] X.B. Mao, S.S. Chen, Chem. Rev. 107 (2007) 2891–2959.
[31] Z. Luo, Q. Gao, J. Photochem. Photobiol. A: Chem. 63 (1992) 367–375.
[32] Y. Wang, H. Cheng, Y. Hao, J. Ma, W. Si, S. Cai, J. Mater. Sci. 34 (1999) 3721–3729.
[33] B. Tian, C. Li, F. Gu, H. Jiang, Y. Hu, J. Zhang, Chem. Eng. J. 151 (2009) 220–227.
[34] C. Adan, A. Bahamonde, M.F. Garcia, A.M. Arias, Appl. Catal. B: Environ. 72 (2007) 11–17.
[35] S.G. Hur, T.W. Kim, S.J. Hwang, H. Park, W. Choi, S.J. Kim, J.H. Choy, J. Phys. Chem. B 109 (2005) 15001–15007.
[36] L.G. Devi, B.N. Murthy, S.G. Kumar, Mater. Sci. Eng. B 166 (2009) 1–6.
[37] L.G. Devi, S.G. Kumar, B.N. Murthy, K. Nagaraju, Catal. Commun. 10 (2009) 794–798.
[38] L.G. Devi, K. Nagaraju, S.G. Kumar, J. Phys. Chem. C 113 (2009) 15593–15601.
[39] L.G. Devi, K. Nagaraju, S.G. Kumar, K.S.A. Raju, Catal. Lett. 131 (2009) 612–617.
[40] Z. Ding, Q. Lu, P.F. Green Field, J. Phys. Chem. B 104 (2000) 4815–4820.
[41] I. Othman, R.M. Mohamed, F.M. Ibrahem, J. Photochem. Photobiol. A: Chem. 189 (2007) 80–85.
[42] J. Lin, J.C. Yu, D. Lo, S.K. Lam, J. Catal. 183 (1999) 368–372.
[43] B. Ohtani, Y. Ogawa, S.I. Nishimoto, J. Phys. Chem. B 101 (1997) 3746–3752.
[44] J. Panpranot, K. Kontapakdee, P. Praserthdam, J. Phys. Chem. B 110 (2006) 8019–8024.
[45] T.V.D. Meulen, A. Mattson, L. Osterlund, J. Catal. 251 (2007) 131–144.
[46] R.R. Basca, J. Kiwi, Appl. Catal. B: Environ. 16 (1998) 19–29.
[47] W. Jun, Z. Gang, Z. Zhaohong, Z. Xiangdong, Z. Guan, M. Teng, J. Yuefeng, Z. Peng, L. Ying, Dyes Pigments 75 (2007) 335–343.
[48] S. Lei, W. Duan, J. Environ. Sci. 20 (2008) 1263–1267.

[49] T. Ohno, K. Sarukawa, K. Tokieda, M. Matsumura, J. Catal. 203 (2000) 82–86.
[50] T. Ohno, K. Tokieda, S. Higashida, M. Matsumura, Appl. Catal. A: Gen. 244 (2003) 383–391.
[51] T. Lopez, R. Gomez, E. Sanchez, F. Tzompantzi, L. Vera, J. Sol–Gel Sci. Technol. 22 (2001) 99–107.
[52] Q. Zhang, L. Gao, J. Guo, Appl. Catal. B: Environ. 26 (2000) 207–215.
[53] K.Y. Jung, S.B. Park, H.D. Jang, Catal. Commun. 5 (2004) 491–497.
[54] Y. Bessekhouad, D. Robert, J.V. Weber, J. Photochem. Photobiol. A: Chem. 157 (2003) 47–53.
[55] Q. Xiao, Z. Si, Z. Yu, G. Qiu, Mater. Sci. Eng. B 137 (2007) 189–194.
[56] Q. Xiao, Z. Si, J. Zhang, C. Xiao, X. Tan, J. Hazard. Mater. 150 (2008) 62–67.
[57] Q. Xiao, Z. Si, Z. Yu, G. Qiu, J. Alloy Compd. 450 (2008) 426–431.
[58] L. Zhao, M. Han, J. Lian, Thin Solid Films 516 (2008) 3394–3398.
[59] B. Sun, P.G. Smirniotis, Catal. Today 88 (2003) 49–59.
[60] G. Li, K.A. Gray, Chem. Phys. 339 (2007) 173–187.
[61] M. Yan, F. Chen, J. Zhang, M. Anpo, J. Phys. Chem. B 109 (2005) 8673–8678.
[62] J.C. Yu, J. Yu, W. Ho, Z. Jiang, L. Zhang, Chem. Mater. 14 (2002) 3808–3816.
[63] J.C. Yu, L. Zhang, J. Yu, Chem. Mater. 14 (2002) 4647–4653.
[64] J.C. Yu, J. Yu, L. Zhang, W. Ho, Chem. Commun. (2001) 1942–1943.
[65] A. Zachariah, K.V. Baiju, S. Shukla, K.S. Deepa, J. James, K.G.K. Warrier, J. Phys. Chem. C 112 (2008) 11345–11356.
[66] Y. Yu, J.C. Yu, J.G. Yu, Y.C. Kwok, Y.K. Che, J.C. Zhao, L. Ding, W.K. Ge, P.K. Wong, Appl. Catal. A: Gen. 289 (2005) 186–196.
[67] J. Yu, M. Zhou, B. Cheng, H. Yu, X. Zhao, J. Mol. Catal. A: Chem. 227 (2005) 75–80.
[68] Y.V. Kolenko, B.R. Churagulov, M. Kunst, L. Mazerolles, C.C. Justin, Appl. Catal. B: Environ. 54 (2004) 51–58.
[69] C. Wu, Y. Yue, X. Deng, W. Hua, Z. Gao, Catal. Today 93–95 (2004) 863–869.
[70] R.I. Bickley, T.G. Carreno, J.S. Lees, L. Palmisano, R.J.D. Tilley, J. Solid State Chem. 92 (1991) 178–190.
[71] D.C. Hurum, A.G. Agrios, K.A. Gray, T. Rajh, M.C. Thurnauer, J. Phys. Chem. B 107 (2003) 4545–4549.
[72] S. Leytner, J.T. Hupp, Chem. Phys. Lett. 330 (2000) 231–236.
[73] X. Hong, Z. Wang, W. Cai, F. Lu, J. Zhang, Y. Yang, N. Ma, Y. Lin, Chem. Mater. 17 (2005) 1548–1552.
[74] G. Li, N.M. Dimitrijevic, L. Chen, J.M. Nichols, T. Rajh, K.A. Gray, J. Am. Chem. Soc. 130 (2008) 5402–5403.
[75] Z. Zhang, C.C. Wang, R. Zakaria, J.Y. Ying, J. Phys. Chem. B 102 (1998) 10871–10878.
[76] Y.V. Pleskov, Sov. Electrochem. 17 (1981) 1–25.
[77] L. Palmisano, V. Augugliaro, A. Sclafani, M. Schiavello, J. Phys. Chem. 92 (1988) 6710–6713.
[78] S.H. Mohamed, J. Phys. D: Appl. Phys. 43 (2010), Article ID 035406.
[79] S.H. Mohamed, J. Phys. D: Appl. Phys. 43 (2010) 1–8.
[80] W. Choi, A. Termin, M.R. Hoffmann, J. Phys. Chem. 98 (1994) 13669–13679.
[81] A.W. Xu, Y. Gao, H.Q. Liu, J. Catal. 207 (2002) 151–157.